ELSEVIER

#### Contents lists available at ScienceDirect

# Acta Materialia

journal homepage: www.elsevier.com/locate/actamat



# Thermodynamically consistent variational principles for charged interfaces



J. Lund<sup>a</sup>, K.S.N. Vikrant<sup>a</sup>, C.M. Bishop<sup>b</sup>, W. Rheinheimer<sup>a</sup>, R.E. García<sup>a,\*</sup>

- <sup>a</sup> School of Materials Engineering, Purdue University, West Lafayette, IN 47907, USA
- <sup>b</sup> Department of Mechanical Engineering, University of Canterbury, Christchurch 8140 New Zealand

#### ARTICLE INFO

Article history: Received 13 June 2020 Revised 18 October 2020 Accepted 23 November 2020 Available online 1 December 2020

Keywords: Charged interfaces Space charge Ideal solution models Strong solution models Conductivity

#### ABSTRACT

A generalized framework that naturally incorporates the free energy contributions of thermochemical, structural, mechanical, and electrical fields is presented to describe the Space Charge Layer (SCL) and their effect on transport properties of ionic ceramics. The theory recovers existing analytical, ideal solution models, such as Debye-Hückel (DH), Mott-Schottky(MS), Symmetric Gouy-Chapman (SGC), and Asymmetric Gouy-Chapman (AGC). Strong solution models, such as Mebane-De Souza (MDS) and Vikrant-Chueh-García (VCG) are discussed. DH, SGC, and AGC models naturally describe the SCL for intrinsic systems, while MS has the capability to capture SCL for substitutional systems with an immobile charged dopant. In general, the ideal solution models fall short in capturing the physical effects associated to SCL in a highly doped system, even though millivolt adjustments to the interfacial voltage decreases the cumulative error associated to experimental electrical conductivity values. In contrast, MDS and VCG models capture very well the concentration-dependent electrical conductivity and contribute a smaller cumulative error, as compared to ideal solution models. Even though MDS provides conductivity fits with uncertainties lower than 0.549%, the defect profiles show sharp, unphysically large concentration gradients, on the order of a few Angstroms. VCG captures the description of a thick SCL, up to 20 nm, due to locally induced chemomechanical stresses, by using physical quantities, delivering uncertainties of 1.79% in total conductivity. The comprehensive theory presented herein sets the stage to model the microstructural evolution of ionic materials and their properties, and enables to design the underlying microstructure under different external fields such as temperature, stress, electrical, magnetic, and chemical stimuli.

© 2020 Acta Materialia Inc. Published by Elsevier Ltd. All rights reserved.

## 1. Introduction

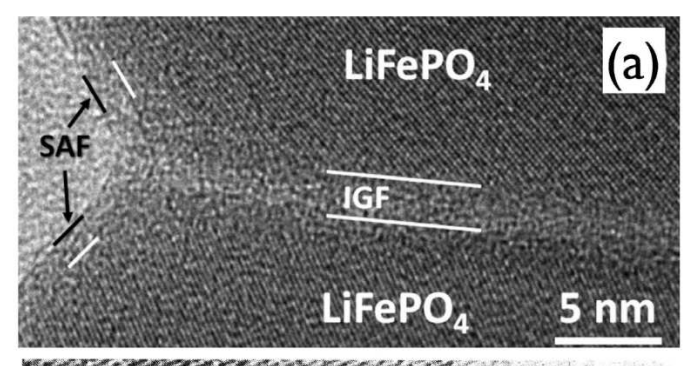
The materials processing, associated microstructural evolution, and resultant performance of currently existing and emerging ion-conducting solids used in sensors, actuators, and energy storage systems, such as SOFCs, lithium-ion batteries, and super-capacitors are controlled, to a first approximation, by the macroscopic composition, and, to a finer level, by the local defect chemistry, particularly at grain boundaries and interfaces. Further, the identification of microstructure-properties relations enables to specify materials processing conditions to obtain the desired local defect chemistry near interfaces, and thus tailor the transport properties to enhance the overall device performance [1–8]. In particular, the solute and

charge distribution in the grain boundary core and its adjacent space-charge during grain growth can be altered by modifying the defect chemistry, temperature, electromagnetic fields, and applied stresses, leading to a wide variety of ionic solids used in energy storage systems and environmentally friendly applications. Specifically, the ionic and electronic conductivity of surfaces and interfaces can differ by several orders of magnitude with respect to the properties of the abutting grains [2,9–11]. In particular, in high electrical conductivity materials, grain boundaries can define a favorable percolation path for charge flow due to their small activation energy for transport [9]; however, in ionic solids, low ionic defect mobility within the grain boundary can result in a nonzero equilibrium charge, which, in turn, can be unfavorable to the through thickness transport properties [12–14].

Grain boundaries form when two crystals of identical composition and structure, but different crystallographic orientations, join during sintering [15]. The difference in orientation sometimes favors the formation of intergranular films, see Fig. 1(a) [7], the

<sup>\*</sup> Corresponding author.

E-mail addresses: lund3@purdue.edu (J. Lund), karras@purdue.edu (K.S.N. Vikrant), catherine.bishop@canterbury.ac.nz (C.M. Bishop), w.rheinheimer@fz-juelich.de (W. Rheinheimer), redwing@purdue.edu (R.E. García).



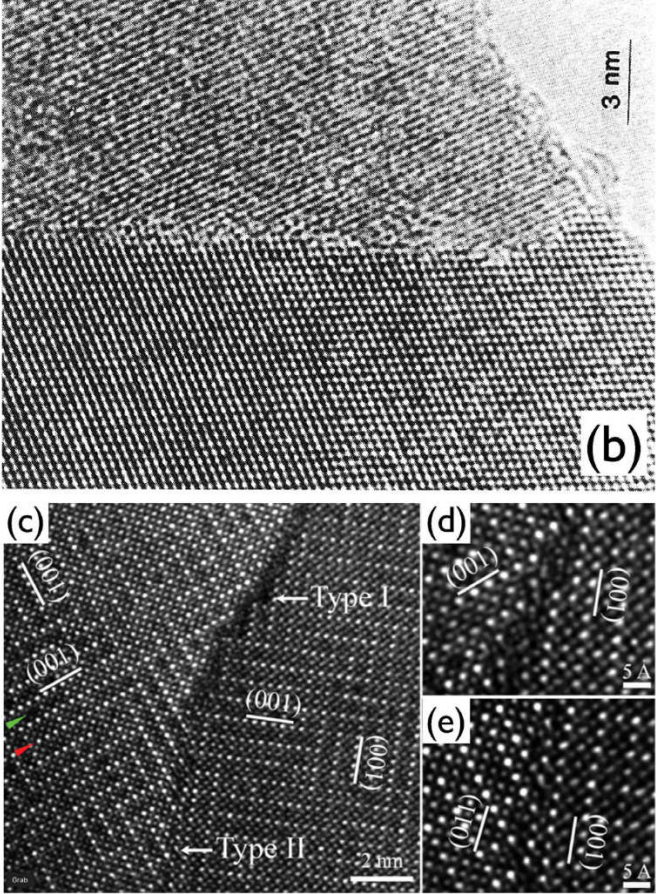


**Fig. 1.** Three example chemistries displaying different types of interfaces: Inset (a) shows a nanoscale intergranular films (IGF), as displayed in LiFePO<sub>4</sub> (LFP) particles, which enhances the overall electrical conductivity [7]. Inset (b) shows a structurally disordered interface in  $(Y_2O_3)_{0.08}(ZrO_2)_{0.92}$ , (8YSZ) with a large segregation of ionic defects, which suppresses the total electrical conductivity [16]. Inset (c) shows two types of interfaces in LiLaTiO<sub>3</sub> (LLTO): Type I, a disordered grain boundary exhibiting large conductivity, and Type II, an ordered grain boundary with poor transport properties. The magnified view of Type I and Type II grain boundaries are shown in inset (d) and (e), [8].

formation of disordered structures with a large segregation of ionic defects, see Fig. 1(b) [16], and even form the different types of grain boundary faceting or disconnections, see Fig. 1(c) through (e), Ma et al. [8], Luo [9], Priester [17]. In ionic ceramics, grain boundaries that favor charged point defects, result in an electrically charged interface [8,18]. If, for example, positively charged defects preferentially accumulate at interfaces, they will attract negatively charged defects in the vicinity of the interface to counteract the interface-induced deviation from charge neutrality [4]. This negatively charged layer is defined as the Space Charged Layer,

SCL, Göbel et al. [4], and extends beyond the structural interface into the bulk of the abutting grains.

Historically, the description of the electrical state of an ionic solid, both for the interface and the bulk, was found by solving Maxwell's Equations [20], specifically, Coulomb's equation in its differential form [20], also known as Poisson's equation [4,12,21]:

$$\epsilon_{\circ} \epsilon_r \nabla^2 \phi + \rho = 0 \tag{1}$$

Here,  $\phi$  is the electrostatic potential,  $\rho$  is the volumetric charge density,  $\epsilon_{\circ}$  is the permittivity of the vacuum, and  $\epsilon_{r}$  is the relative dielectric constant for the material [3,4,20]. All symbols used in this paper can be found in the Table of Symbols in Appendix A. Typically, in published models,  $\epsilon_{r}$ , the material relative permittivity, is assumed a material constant, even though the interfacial permittivity is known to differ from the bulk due to structural differences [1,4,22–25].  $\rho$  is a function of the contributions to the spatial charge distribution from intrinsic and extrinsic species,

$$\rho = \sum_{i=1}^{N} \frac{\mathcal{F}Z_{i}y_{i}}{\nu_{i}} \tag{2}$$

where  $\mathcal{F}$  is Faraday's constant,  $Z_i$  is charge number or valence,  $\nu_i$  is molar volume density of the sublattice where *i*th defect resides, and  $y_i$  is site fraction of the *i*th chemical species.

Without any loss of generality, define the grain boundary region as a space contained within the yz plane in a Cartesian (right handed) coordinate system, while the normal of the interface is parallel with the x-direction. In the absence of ferroelectricity, for an interface at equilibrium, assume that the extended multiphysical fields away from the boundary are the same when measured at the same distance from the interface on both sides: they are symmetrically distributed [1], and historically solved for x > 0. Thus, the description of the grain boundary plus surrounding grains is reduced to a one dimensional (1D) system by considering the normal distance from the grain boundary core. Also historically, the grain boundary has been treated as an infinitely thin region in space at x = 0. Typically, the fields at the grain boundary core are considered a boundary condition for the abutting surrounding grains, even though experimental evidence demonstrates that the properties of polycrystalline ceramics are a result of the local thermodynamic equilibrium that develops between grains and grain boundaries, as demonstrated by Gibbs [26], and later Cahn [27,28]. The historical set of 1D solutions are applicable as long as the extent of the region of influence of the interface is much smaller than the grain size or the next closest grain boundary [29,30].

The thermodynamic [31], and phase field [32,33], communities describe polycrystalline ceramics by defining the *thermochemical* Helmholtz free energy per unit volume, f, as a function of M phases described by a set of order parameters,  $\{\eta_j\} = \{\eta_1, \ldots, \eta_M\}$ , N charged species having a site fraction,  $\{y_i\} = \{y_1, \ldots, y_N\}$ , and Q sublattices described by  $\{q_1 \ldots q_Q\}$  each contributing to the entropic and enthalpic free energies of mixing through expressions of the form

$$f(\{y_i\}, \{\eta_j\}, T) = \sum_{i=1}^{N} \frac{1}{\nu_i} \left( f_i(\{\eta_j\}, T) y_i + RT y_i \ln y_i \right)$$

$$+ \sum_{q=1}^{Q} \frac{RT}{\nu_q} \left( 1 - \sum_{i=q}^{N} y_i \right) \ln \left( 1 - \sum_{i=q}^{N} y_i \right) + \Delta H_{mix}(\{y_i\}, T)$$
 (3)

where R is the universal gas constant, T the absolute temperature, and  $\Delta H_{mix}^{-1}$  the excess enthalpy energy of mixing including all non-ideal contributions from the local thermochemical interactions between the different ionic components. Additionally,  $f_i$  is a

<sup>&</sup>lt;sup>1</sup> In the literature,  $\Delta H_{mix} = \Delta G_{mix} + T \Delta S_{mix}$ 

combination of the formation energies of *i*th defect in all phases present, including any that may only form metastably within the grain boundary [9]. Here, in thermodynamics-based constructions, the material energetically favors chemical attraction to the grain boundary of those ionic components that minimize the interfacial energy of the system [32,34,35].

The description of the interaction energetics found in Eq. (3) requires, to a first approximation, to split the lattice into cation and anion sites, in terms of a sublattice model. Each ith species has a site fraction,  $y_i$ , for each sublattice, in agreement with Sundman and Ågren [36], enabling sublattice-sublattice interactions to be considered. For non-ideal systems, i.e.,  $\Delta H_{mix} \neq 0$ , the simplest non-ideal description corresponds to a regular solution model, i.e.,

$$\Delta H_{mix}(\{y_i\}, T) = \sum_{i,j=1, i \neq j}^{N} \frac{\Omega_{ij} y_i y_j}{\nu_i} \text{ for ionic interfaces [37], and ac-}$$

counts for the pair-wise chemical interactions between each of the defects. Here, the self-interaction energy of the ith defect on a sublattice,  $\Omega_{ii}=0$  in a regular solution model [36]. This follows from the definition of the enthalpy of mixing for a regular solution and the assumption of random mixing of defects. The description of higher order interactions of ion-defect and defect-defect in a sublattice is formulated using clustering entropy models [38].

From classical thermodynamics, the differential of the Helmholtz free energy density is  $df = \sum_{i}^{N} \mu_{i} \frac{y_{i}}{\nu_{i}} - s dT + \phi d\rho$ , where  $\mu_{i}$  is chemical potential of ith defect, and s is entropy density. By combining Eqs. (2) and (3), in the dilute limit,  $\ln(1-\sum_{i=1}^{N}y_{i}) \rightarrow 0$ , and for a single phase of an ideal solution,  $\Delta H_{mix} = 0$ , the classic electrochemical potential,  $\tilde{\xi}_{i}$  is defined as, [39]. [40],

$$\tilde{\xi}_i = f_i(T) + RT \ln y_i + Z_i \mathcal{F} \phi \tag{4}$$

At equilibrium, the local electrochemical potential of the ith species,  $\tilde{\xi}_i$  is equal to the far field electrochemical potential of the ith species,  $\tilde{\xi}_{i,\infty}$ , i.e.,  $\tilde{\xi}_{i,\infty}i(x\to\infty)=\tilde{\xi}_{i,\infty}$ . Assuming,  $y_i(x\to\infty)=y_{i,\infty}$ , [1,4,30,41,42,43,4445,46], and by defining the electrostatic potential relative to the bulk, i.e.,  $\phi_\infty=0$ , the site fraction of the charged species is obtained as a function of local electrostatic potential through the expression:

$$y_{i} = y_{i,\infty} \exp\left(-Z_{i} \mathcal{F} \phi / RT\right) \tag{5}$$

The scientific communities attempt to describe the same materials through very different means, by substituting the physically simplified (ideal solution), Eq. (4) into Eq. (2) and then further into Eq. (1), which has allowed to propose models to rationalize the properties in the vicinity of the interface. In this paper, a continuum thermodynamic treatment based on a free energy density is used to describe the extended electrochemical state of a grain boundary and its local surroundings. The proposed framework generalizes ideas originally proposed by Cahn, Hart, and Penrose [47–50], and has been applied to electrochemical systems by Guyer [51,52], and the authors of this work [37,53,54]. It allows to formulate advanced physical descriptions with thermodynamically consistent mechanisms. In the asymptotic ideal solution limit, the proposed variational framework reduces to classic descriptions. The proposed formulation is a function of the controlling physical variables of the system [50,53], and allows for a direct comparison against experimentally measurable quantities as e.g., conductivities or grain boundary migration rates.

## 2. Variational framework

For an ionic solid, define the volumetric free energy of the system,  $f_{vol}(\{y_i\}, \{\eta_j\}, \rho, \vec{D}, T) = f(\{y_i\}, \{\eta_j\}; T) + \rho\phi + \frac{1}{2}\vec{D} \cdot \vec{E}$ .

Here, the volumetric Helmholtz free energy increases when the local charge density,  $\rho$ , has the same sign as the electrostatic potential,  $\phi$ , while the third term, the dipolar energy density, penalizes the increase of electrostatic energy when an electric field,  $\vec{E}$ , is induced by a nearby electrostatic charge or externally imposed by the boundary condition. The Legendre transformation defines the electrochemical free energy density,  $f_{ec}(\{y_i\}, \{\eta_i\}, \rho, \vec{E}, T) = f_{vol}(\{y_i\}, \{\eta_i\}, \rho, \vec{D}, T) - \vec{D} \cdot \vec{E}$ , in agreement with previous work [26,51,53-55]. In addition, the electrostatic potential and the electric field are related through the relation,  $\vec{E} =$  $-\nabla \phi$ , because the position-dependent electric field is a solution of Faraday's Law,  $\nabla \times \vec{E} = \vec{0}$ , for a constant magnetic induction field [20]. Lastly, the electric displacement vector and the electric field are related through the constitutive equation,  $\vec{D} = \epsilon_0 \epsilon_r \vec{E}$ , in the absence of piezoelectric and pyroelectric effects [20]. In agreement with Hart [49], and recent work [18,37,53,54,56], the total free energy of the system, F, is:

$$F[\{y_i\}, \rho, \phi, \{\eta_j\}, \{v_k\}; T]]$$

$$= \int_V \left( f(\{y_i\}, \{\eta_j\}, T) + \rho \phi - \frac{1}{2} \epsilon_{\circ} \epsilon_r (\nabla \phi)^2 \right) dV$$

$$+ F_{add}[\{y_i\}, \phi, \{\eta_j\}, \{v_k\}; T]$$
(6)

Here, V is the total volume of the system, and  $\{\eta_i\}$  correspond to a set of order parameters, each defining a material phase [32,57]. For example,  $\eta_1$ , represents a continuous transformation from an ordered, crystalline structure,  $\eta_1 = 1$ , to a completely crystallographically disordered structure or phase,  $\eta_1 = 0$ . The second term of Eq. (6),  $F_{add}$ , corresponds to an additional free energy contribution to the system that goes beyond the traditional volumetric electrochemical or thermochemical driving forces, such as interfacial energy contributions, mechanical energy. $v_k$  corresponds to the kth controlling variable describing other volumetric thermodynamic driving forces for phase transformation and are represented by the set of order parameters,  $\{v_k\}$ . Specific forms of  $F_{add}$ have been proposed by Cahn in his seminal work, [27,28,47,48], or its extensions to multiphysical systems [37,51,53,58], and microstructural evolution [27,28,47,48,59-61]. Specific examples include [1,19,47], as well as those that aim to include the effects of mechanical stresses [2,37], or interfacial ion adsorption [62].

The local equilibrium conditions of the polycrystalline system correspond to the minimum of F subjected to boundary conditions and is related to the generalized thermodynamic potentials defined by the variational derivatives of Eq. (6):

$$\frac{\delta F}{\delta \phi} = \epsilon_{\circ} \epsilon_{r} \nabla^{2} \phi + \rho + \frac{\delta F_{add}}{\delta \phi} = 0$$

$$\frac{\delta F}{\delta \eta_{j}} = \frac{\partial f}{\partial \eta_{j}} + \frac{\delta F_{add}}{\delta \eta_{j}} = 0$$

$$\frac{\delta F}{\delta y_{i}} = \frac{\partial f}{\partial y_{i}} + \frac{Z_{i} \mathcal{F}}{\nu_{i}} \phi + \frac{\delta F_{add}}{\delta y_{i}} = \xi_{i}$$

$$\frac{\delta F}{\delta \nu_{k}} = \zeta_{k} \tag{7}$$

The first row of Eq. (7) corresponds to Coulomb's equation (Eq. (1)), in agreement with the classical electromagnetics literature [20], and previous work [51,53,54]. The second row embodies the effect of the set of order parameters,  $\{\eta_j\}$ , on the local stability of the spatially coupled grain boundary-grain system, and defines their equilibrium and phase transition conditions [37,63–66]. The third row corresponds to the generalized electrochemical potential,  $\xi_i$ , of the i-th ionic species and reduces to its classic form (Eq. (4)) in the limit of a single phase system [51,53,54]. Finally, the last row corresponds to the generalized contribution of the k-th potential,  $\zeta_k$ , as a result of the variational derivative with respect to its controlling variable,  $v_k$ . Eq. (7) defines a generalized local thermo-

dynamic driving force for mass segregation at interfaces as a result of gradients of chemical potential, electrostatic potential, or generalized order parameters, and enables to formulate space charge layer models.

## 3. Space charge layer models

#### 3.1. Ideal solution models

In all the ideal solution models, additional contributions to the free energy in Eq. (6),  $F_{add}=0$  because there are no underlying phase transitions or additional physical driving forces. Thus, the only controlling variables are the electrostatic potential,  $\phi$ , and the concentration of defects,  $y_{\rm j}$ . Other contributions to the free energy that are function of order parameters,  $\eta_{\rm j}$ , and controlling variables,  $v_k$ , are negligible. Therefore, the second and fourth rows of Eq. (7) are trivially satisfied, and are thus ignored. In the dilute defect concentration limit, the third row of Eq. (7) results in Eq. (5). Specifically, the first row of Eq. (7) reduces to the Debye-Hückel model (DH) [46,67,68], also known as the Dilute Gouy-Chapman model [56], in the dilute defect concentration limit (see Appendix B.1 and B.2 for details). Specifically, for high temperatures and low electrostatic potentials,  $\mathcal{F}\phi(x)/RT \ll 1$ , Eq. (5) is approximated as  $y_i = y_{i,\infty}(1-Z_i\mathcal{F}\phi(x)/RT)$ , reducing the first row in Eq. (7) to

$$\frac{d^2\phi(x)}{dx^2} = \frac{\phi(x)}{\lambda_{Dh}^2} \tag{8}$$

where

$$\lambda_{\text{Db}} = \sqrt{\frac{\epsilon_{\circ} \epsilon_{r} RT}{\mathcal{F}^{2} \sum_{i=1}^{N} Z_{i}^{2} y_{i,\infty} / \nu_{i}}}$$

$$(9)$$

is known as the Debye length [1]. Define  $\phi(x=0)=\phi_\circ$ , as the electrostatic potential at the grain boundary core. Thus, the analytical solution of Eq. (8) is  $\phi(x)=\phi_\circ\exp(-x/\lambda_{\rm Db})$ , the electrostatic potential distribution away from the grain boundary. DH shows that grain boundaries influence the defect concentrations in the SCL and defines a measure for the extent of the SCL. Although DH is not commonly used today, the Debye length is a popular measure of the extent of the space charge due to the ease with which the parameters in Eq. (9) are obtained experimentally [56,62,69–72].

Based on the same concepts, Mott [44,45] and Schottky [73] developed a model (MS) to describe a heterogeneous interface between a metal and a semiconductor, and account for the effects of the resultant charge accumulation due to the differing electron electrochemical potential affinities of the materials. The MS model has since been applied to describe the effect of a dominant immobile charge carrier in the SCL on the spatial extent of the electrostatic potential and the intrinsic defect concentrations [1]. In this context, the first row in Eq. (7) reduces to (see Appendix B.3 for details):

$$\frac{d^2\phi(x)}{dx^2} = -\frac{\mathcal{F}Z_{im}y_{im}}{v_{im}\epsilon_0\epsilon_r}$$
 (10)

whose analytical solution is:

$$\phi(x) = \begin{cases} \phi_{\circ} \left(\frac{x}{\lambda^*} - 1\right)^2, & x \le \lambda^* \\ 0, & x > \lambda^* \end{cases}$$
 (11)

and

$$\lambda^* = \lambda_{\text{Db}} \sqrt{\frac{4|Z_{im}\phi_{\circ}|\mathcal{F}}{RT}}$$
 (12)

MS remains a popular analysis for doped systems to predict space charge layers in the presence of immobile charge carriers of valence  $Z_{im}$  [4,74,75].

The model developed by Gouy [43] and Chapman [42] considered the interactions at the liquid-solid interface, but has since been extended to describe intrinsic systems in ionic ceramics [1,4,9]. In the symmetric Gouy-Chapman model (SGC), DH is extended to describe the effect of two intrinsic defects of equal but opposite charge, Z and -Z. Thus for  $c_{\infty} = \frac{y_{+,\infty}}{\nu_{+}} = \frac{y_{-,\infty}}{\nu_{-}}$ , Eq. (7) becomes

$$\frac{d^{2}\phi(x)}{dx^{2}} = -\frac{\mathcal{F}}{\epsilon_{\circ}\epsilon_{r}} \left( Zc_{\infty} \exp\left(\frac{Z\mathcal{F}}{RT}\phi(x)\right) - Zc_{\infty} \exp\left(-\frac{Z\mathcal{F}}{RT}\phi(x)\right) \right)$$
(13)

whose analytical solution is [3,4,30,69], (see Appendix B.4 for details):

$$\phi(x) = -\frac{2RT}{Z\mathcal{F}} \ln \left( \frac{1 + \theta \exp(-x/\lambda_{Db})}{1 - \theta \exp(-x/\lambda_{Db})} \right), \quad \theta = \frac{\exp\left(-\frac{Z\mathcal{F}}{2RT}\phi_{\circ}\right) - 1}{\exp\left(-\frac{Z\mathcal{F}}{2RT}\phi_{\circ}\right) + 1}$$
(14)

Eq. (14) is used to approximate a wide variety of situations [30,76]. SGC model has become more popular than DH for intrinsic systems [3,4,69], as its simplifying assumptions result in better conductivity predictions than DH [71].

An asymmetric extension of the symmetric Gouy-Chapman (AGC) ignores the effect of one of the defects and considers one mobile carrier with formal charge  $Z_m$  [4]. Its analytical solution is:

$$\phi(x) = \begin{cases} \phi_{\circ} + \frac{2RT}{Z_{m}F} \ln\left(1 + \frac{x}{2\lambda_{Db}} \exp\left[-\frac{Z_{m}F}{2RT}\phi_{\circ}\right]\right) & x \le 2\lambda_{Db} \\ 0, & x > 2\lambda_{Db} \end{cases}$$
(15)

This simplification works well for intrinsic systems [4]. AGC is used instead of SGC when each charge carrier needs to be treated independently, *e.g.*, when one charge carrier dominates over dilute ones [4]. This has also led to two-dimensional model extensions (parallel and perpendicular to the grain boundary) [30]. For most of the 20th century, these four models were the basis to analyze charged grain boundaries in ionic ceramics [1].

#### 3.2. Strong solution models

Recently, Mebane and De Souza contributed a model (MDS) based on a free energy penalty for concentration gradients to remove the dilute limit assumption that was added to the additional free energy [19]:

$$F_{add}[\{y_i\}; T] = \int_V \left( \sum_{i=1}^N \frac{\alpha_i}{2} (\nabla y_i)^2 \right) dV$$
 (16)

where  $\alpha_i$  are the gradient energy coefficients, as introduced by Cahn and Hilliard to describe the spinodal decomposition for metallic systems [27]. In MDS, the regular solution-like defect interaction parameters and the gradient energy coefficients are treated as fitting parameters to reproduce the experimentally measured ionic conductivity in gadolinium-doped cerium oxide (GCO).<sup>2</sup> The dopant-vacancy interaction energy was fitted to reproduce the peak conductivity as observed by Tschöpe and coworkers [77]. MDS assumes the interface to be atomically sharp and imposes the interfacial boundary condition,  $\frac{\alpha_i}{\nu_i} \frac{dy_i}{dx} \Big|_{x=0} = \frac{(f_i^c - f_i^\infty)}{\nu_o}$  at x=0, with  $y_i=y_{i,\infty}$  in the limit of  $x\to\infty$ .  $f_i^\infty-f_i^\infty$  is the segregation energy of the ith defect and  $\nu_o$  is the area-specific molar

<sup>&</sup>lt;sup>2</sup> Typically gradient energy terms are used for spinodally decomposing systems and the phase separation of materials [27].

site density at the grain boundary, thus establishing an interfacial boundary condition, in agreement with the classic models. MDS delivers large defect concentrations in highly-doped systems and reports a space charge layer two to three times longer than the Debye length, (see Appendix B.5 for details).

Vikrant, Chueh, and García developed a model (VCG) with a regular solution thermo-chemical free energy and formulated the additional free energy contribution to the functional as the elastic energy density,  $\frac{1}{2} \stackrel{\leftrightarrow}{\sigma} \stackrel{\leftrightarrow}{\epsilon} \stackrel{\leftarrow}{\epsilon} [37]$ :

$$F_{add}[\{y_i\}, \vec{u}; T] = \int_V \left(\frac{1}{2} \stackrel{\leftrightarrow}{\sigma} \cdot \stackrel{\leftrightarrow}{\varepsilon}_e\right) dV$$
 (17)

where  $\vec{u}$  is the mechanical displacement vector,  $\stackrel{\leftrightarrow}{\sigma}$  is the stress tensor, and  $\stackrel{\leftrightarrow}{\varepsilon}_e$  is the elastic strain tensor. Specifically,  $\varepsilon_{kl,e}$  =

$$\left( \varepsilon_{kl} - \sum_{m=1}^N \beta_{kl}^m ({\sf y_m} - {\sf y_{m,\circ}}) \right)$$
 is the  $kl$ th component of elastic strain

tensor and 
$$\sigma_{ij} = C_{ijkl} \varepsilon_{kl,e} = C_{ijkl} \left( \varepsilon_{kl} - \sum_{m=1}^{N} \beta_{kl}^{m} (y_m - y_{m,o}) \right)$$
 is the

ijth component of the elastic stress tensor, all of which are directly measurable quantities. Here,  $C_{ijkl}$  is the ijklth component of stiffness tensor,  $\varepsilon_{kl}$  is klth component of total (or geometrical) strain,  $\beta_{kl}^m$  is klth component of the Vegard tensor of the mth species, and  $y_{m,\circ}$  is the stress-free concentration of mth species.

The free energy of formation of chemical species in Eq. (3) is described as:

$$f_{i}(\eta, T) = f_{i}^{\circ}(T)p(1 - \eta) + f_{i}^{\infty}(T)p(\eta)$$
(18)

where  $f_i^\circ$  is the grain boundary formation energy of the ith species, and  $f_i^\infty$  is formation energy in the bulk of the crystal.  $\eta$  represents a structural order parameter, which is 1 in crystalline structure, and is 0 in crystallographically disordered region.  $p(\eta) = \eta^3(6\eta^2 - 15\eta + 10)$  is an interpolation function. Here, the structural disorder in the grain boundaries naturally accumulates or depletes point defects and ionic species based on the segregation energy differences,  $f_i^\circ - f_i^\infty$ . With this framework, VCG captures the electrochemical, structural and chemomechanical state of a grain boundary and its abutting grains which allows to physically describe the equilibrium and transport properties of polycrystalline ionic ceramics (see Appendix B.6 for details).

## 4. Application to gadolinia-doped ceria

#### 4.1. Material and numerical generalities

For this paper, gadolinium-doped cerium oxide (GCO), a wellstudied cubic material system [1,3,77-80,80-82], was selected as a test material. In the present study, the major defects considered are  $Gd'_{Ce}$  and  $V'_{O}$ . GCO has high bulk ionic conductivity [81], but is limited by its grain boundary conductivity. Additionally, GCO is sometimes heavily-doped, which breaks the assumptions established for the historical models and highlights the need for strong-solution models. Experimental results reported that grain sizes ranged between 0.5 and 5 µm, with an average grain size of 1 µm [77]. For the calculations performed herein, polycrystals were assumed to have a grain size of 1 µm. As the SCL length is much smaller than 500 nm, the assumption of noninteracting SCL holds. Gadolinium site fractions between 0.01 and 0.3 were modeled, with oxygen vacancies as the charge compensating defect. Other defects, such as electrons and holes, were ignored. Ionic conduction is assumed to occur solely through oxygen vacancy motion alone. Thus, lower oxygen vacancy concentrations result in lower conductivities.

A two-grain system with a planar grain boundary was modeled by placing the interface (the grain boundary plane) at the origin of

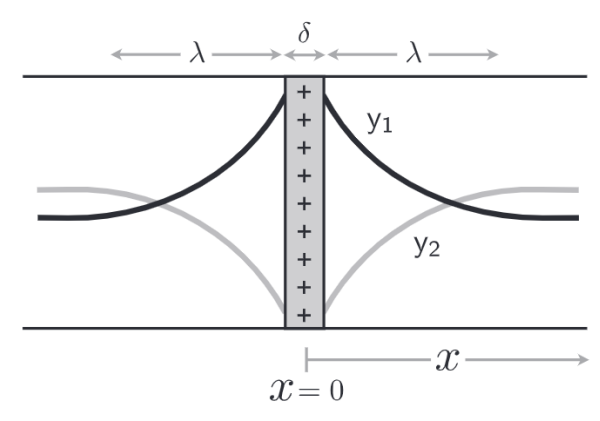


**Fig. 2.** Schematic of charged defect distribution in the vicinity of grain boundary of thickness,  $\delta$ . The simulation domain is 20 nm. An SCL of characteristic extent,  $\lambda$ , corresponds to a symmetric region abutting the interface, where the concentration of ionic species deviates from the bulk values. Charge distribution symmetry enables to focus on one side (e.g., x>0) away from the interface. Thus, for a positively charged interface and two oppositely charged point defect site fractions,  $y_1$  and  $y_2$ , if  $y_2$ , has a positive charge, it will deplete in the SCL, and  $y_1$ , with a negative charge will accumulate in the SCL, given a set of far field concentrations,  $y_{1,\infty}$  and  $y_{2,\infty}$ .

the laboratory reference system (at x=0), as shown in Fig. 2. The normal of the interface was arbitrarily set to point along the x-axis. For the ideal solution models, the interface was considered as atomically sharp, *i.e.*,  $\delta=0$ . Because of the symmetry of the bicrystal, the right edge of the grain was set to be electrically grounded, while chemically the defect site fractions were set based on the amounts of dopant concentration. At x=0, the voltage was set to the Schottky potential,  $\phi=\phi_{\rm o}$ . The defect profiles for all ideal solution models were obtained by using Eq. (5). For the DH, and MS models, the electrostatic potential distribution was solved by using Eqs. (8) and (10) in Mathematica, [83]. For the SGC, the voltage profile was obtained by using Eq. (14). Similarly, for the AGC, the voltage profile was obtained by using Eq. (5).

In the case of the strong solution models, the MDS model assumes the interface to be atomically sharp, i.e.,  $\delta = 0$ . The right edge of the simulation domain was electrically grounded, while the defect site fractions were set to be equal to the macroscopic dopant concentration. At x = 0, a boundary condition was imposed in terms of segregation energy,  $(f_i^{\circ} - f_i^{\infty})$ , through the expression:  $\frac{\alpha_i}{\nu_i}\frac{dy_i}{dx}\Big|_{\chi=0}=\frac{(f_i^\circ-f_i^\infty)}{\nu_\circ}$ . Equation set (7) was solved across a 20 nm simulation domain, and discretized into a 200 finite element mesh using an iterative Newton's method implemented in Matlab, as available in the literature [19,84]. For the VCG model, the degree of order of the structure,  $\eta$ , was set to the analytical solution  $\eta = 1 - (1 - \eta_{\circ}) \exp[-||x||/\delta]$ , in agreement with the phase field literature [34,35]. Here,  $\eta_0 = 0$  is the order in the grain boundary and the thickness of the grain boundary was set to  $\delta = 2$  nm. The right edge of the simulation domain was set to be electrically grounded and the defect site fractions were set based on the macroscopic amounts of dopant concentration. Because of the symmetry of the two-grain system, the horizontal mechanical displacement at the center of the grain boundary was set to be zero, while set to expand freely in the vertical direction. Equation set (7) and the mechanical equilibrium equation,  $\nabla \cdot \stackrel{\leftrightarrow}{\sigma} = \stackrel{\leftrightarrow}{0}$ , were solved across a  $20 \times 20$  nm simulation domain and discretized into a 200 x 200 finite element mesh. The mechanical equilibrium equation was solved using OOF2 under plane-stress conditions by using a Bi-Conjugate Gradient solver with an ILU preconditioner [85]. The relative tolerance for convergence was set to  $1 \times 10^{-8}$ . The electrochemical parts of the partial differential equations were solved by using FiPy with a Linear PCG solver [86]. The

relative tolerance for convergence was set to  $1\times 10^{-8}$ . Each calculation took on the order of two hours of wall time to complete in a 2.6 GHz, 16 core, Ubuntu 16.04 workstation machine with 128 GB of RAM.

A brick resistor-network model was used to calculate the conductivity as described by Guo [12]. The single crystal conductivity is assumed to be due to the contribution of major carriers, in this case, the oxygen vacancies. All used parameters are summarized in Table 1. The total conductivity,  $\kappa$ , is given by the sum of the contributions to resistivity across a representative grain boundary [12,37]:

$$\frac{1}{\kappa} = \frac{1}{L} \int_{0}^{L} \frac{dx}{\sum_{i=1}^{N} \frac{e^{2} Z_{i}^{2} y_{i}^{2} D_{i}^{\circ}}{k_{B} T}} \exp\left(-\frac{E_{a,i}(y_{i})}{k_{B} T}\right)$$
(19)

where L is the grain size and  $k_B$  is Boltzmann constant. The pre-exponential constant for self-diffusion coefficient,  $D_{\text{V}_{\text{O}}}^{\circ} = 0.001 \, \text{m}^2/\text{s}$ , and its activation energy,  $E_{a,\text{V}_{\text{O}}^{\circ}} = 2.4525\text{y}_{\text{V}_{\text{O}}^{\circ}} + 0.7629 \, \text{eV}$ , were fitted to the single crystal conductivity [77]. An adaptive mesh scheme NIntegrate, as implemented in Mathematica [83], was used to compute the electrical conductivity for the ideal solution models. The three orders of magnitude level of resolution discretization for the large variations in concentration near the grain boundary were spatially resolved. The strong solution models are solved numerically in the original work, and the code published by the respective authors was used .

The deviation between experiment and numerical model was computed through the expression:

$$err = \sqrt{\frac{\sum_{i=1}^{n} \left(\log(\kappa^{exp}(y_i)) - \log(\kappa^{model}(y_i))\right)^2}{n}}$$
 (20)

where err is root mean square error, n is number of measurements, and  $y_i$  is the dopant site fraction, as reported by Tschöpe and coworkers [77]. For those calculations that optimized the conductivity for each of the models, Eq. (20) was minimized. The concentration gradient energy parametric analysis was performed by modifying the VCG model, removing the elastic energy contributions. The resulting optimized values are summarized in Table 2.

## 4.2. Results and discussion

Fig. 3 compares the GCO conductivity predictions against experimental data for each model, based on the input parameters of Table 1, which correspond to experimental data reported in the literature [77]. The reported grain boundary voltages,  $\phi_{\circ}$ , range between 0.14 and 0.5 V [87–92]. Experimental results show that grain boundaries suppress the electrical conductivity regardless of gadolinium content [77]. Further, at large defect concentrations, the contributions from the SCL to conductivity are less dominant as compared to the grains, thus all models eventually converge to describe the single crystal behavior. Additionally, an increase in gadolinium site fraction increases oxygen vacancy concentration, which, in turn, increases the electrical conductivity up to a maximum value of  $1.57 \times 10^{-3}$  S/cm.

Because the chemical interactions between the different species in the ideal solution models were ignored, they fall short in predicting the electrical conductivity at large defect concentrations. Specifically, SGC assumes point defects with equal and opposite charges, which is not satisfied by  $V_O^*$  and  $Gd_{Ce}^\prime$ . At low defect concentrations, this causes an over prediction of conductivity. Conversely, AGC ignores the effects of extrinsic defects, and thus under predicts the electrical conductivity. Similarly, both the

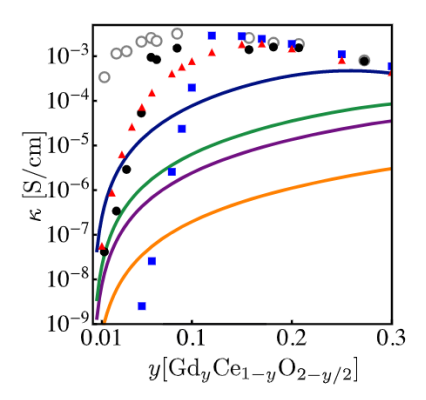


Fig. 3. Macroscopic ionic conductivity as a function of dopant concentration in GCO for each described model using parameters in Table 1. Experimental data corresponds to ○ for single-crystal GCO and ○ for polycrystalline GCO [77]. Model results correspond to ─ for DH, ─ for MS, ─ for SGC, ─ for AGC, ○ for MDS, and ○ for VCG. AGC shows large conductivity losses at intermediate and large dopant concentrations. The predicted polycrystalline conductivity values using ideal solution models are three orders of magnitude smaller than the experimental values at intermediate dopant concentrations. The MDS model under-predicts polycrystalline conductivity given the resistor-network description. VCG correctly predicts at low and high dopant concentrations, but does not show the maximum conductivity as seen experimentally.

DH and MS models fail to predict the maximum experimental conductivity value. Thus, for y > 0.05, none of the ideal solution models are valid. The MDS model reproduces the experimental conductivity for y > 1.5 and successfully predicts the orders-of-magnitude smaller electrical conductivity value at low dopant concentrations [19,93].

The VCG model reproduces the experimental result very well across the entire range of dopant compositions. The authors believe that the small differences are a result of the higher order thermochemical interactions and additional chemomechanical non-linearities that require a finer level of multiphysical description. Also, the authors successfully extended the VCG model to explain the interfacial phase transitions in ionic ceramics by incorporating the effect of crystallographic misorientations and their impact on electrical conductivity [29], something that is limiting in MDS because it was not developed to track interfaces. In this context, the approach layed down by VCG sets the stage to rationalize the microstructural evolution during grain coarsening and charge transport in a sintering process under an external applied field [94–98].

To provide an equal footing point comparison for each model, the parameters were freely allowed to vary to be optimized to fit the experimental data, see Table 2. The predicted electrical conductivity for these optimized parameters is shown in Fig. 4. For the ideal solution models, millivolt adjustments to the grain boundary voltage delivers nearly the same predicted electrical conductivity value, improving it within an order of magnitude of the experimental results for all reported gadolinium site fractions. However, even though the ideal solution models appear to show the correct electrical conductivity trend, the analysis shows that it is very easy to impose non-physical boundary conditions and unphysical parameters, e.g., the gradient energy coefficients for defects [99], and models such as MS and AGC have contradictory assumptions, highlighting that only one or neither, can have physical representations of the actual material system.

The MDS model optimization was performed using the same resistor-network conductivity model in Eq. (19). Its cumulative error is the lowest of all the models (see Table 3), and is able to successfully capture the maximum conductivity. However, as with the ideal solution models, this does not imply that the description is physical. The effect of different additional free energy contribu-

**Table 1** Summary of material parameters for GCO based on literature. Note that all the ideal solution models used the same parameters. Here,  $^{\ddagger}$  denotes a fitting parameter used to match experimental data for the models, and  $^{\dagger}$  denotes MDS model used a fitting parameter, not reported in literature.

Symbol	DH, MS, SGC, AGC	MDS	VCG	Units	Ref
Е	_	_	190	GPa	[80]
$f_{\mathrm{Gd'_{Ca}}}^{\circ} - f_{\mathrm{Gd'_{Ca}}}^{\infty}$	_	0.0	0.0	eV/atom	-
$f_{\mathrm{Gd'_{Ce}}}^{\circ} - f_{\mathrm{Gd'_{Ce}}}^{\infty} \ f_{\mathrm{V_{0}}}^{\circ} - f_{\mathrm{V_{0}}}^{\infty}$	_	-2.0	-2.0	eV/atom	[77,79]
L	$0.5 \times 10^{-6}$	$0.5 \times 10^{-6}$	$0.5 \times 10^{-6}$	m	[77]
T	440	440	440	°C	[77]
$Z_{\mathrm{Gd}}$	-1	-1	-1	_	-
$Z_{\rm O}$	+2	+2	+2	-	_
$\alpha_{a}$	_	2.5 <sup>‡</sup>	_	eV nm²	_
$\alpha_{ extsf{v}}$	_	$0.125^{\ddagger}$	_	eV nm²	_
$\beta_T$	_	_	0.00095	_	[81]
δ	_	_	2 <sup>‡</sup>	nm	_
$\epsilon_r$	35	35	35	_	[78]
ν	_	_	0.3	_	[80]
$v_{Gd}$	$2.409 \times 10^{-5}$	$2.419 \times 10^{-5}$	$2.409 \times 10^{-5}$	mol/m <sup>3</sup>	[19]
$v_0$	$1.205 \times 10^{-5}$	$1.209 \times 10^{-5}$	$1.204 \times 10^{-5}$	mol/m <sup>3</sup>	[19]
$\nu_{\circ}$	_	$2.6 \times 10^{-5}$	_	mol/m <sup>2</sup>	[77]
$\eta_{\circ}$	_	_	$0_{\ddagger}$	_	_
$oldsymbol{\phi}_\circ$	0.3 <sup>‡</sup>	_	_	V	[87]
$\Omega_{\mathrm{Gd'_{Ce}}\mathrm{Gd'_{Ce}}}$	_	0.1	_	eV/atom	[79]
$\Omega_{\mathrm{Gd'_{Ce}V_{O}^{"}}}$	_	$-0.07^{\dagger}$	-0.3	eV/atom	[79]
$\Omega_{V_0^-V_0^-}$	_	0.9	_	eV/atom	[79]

coefficients, similar to MDS.

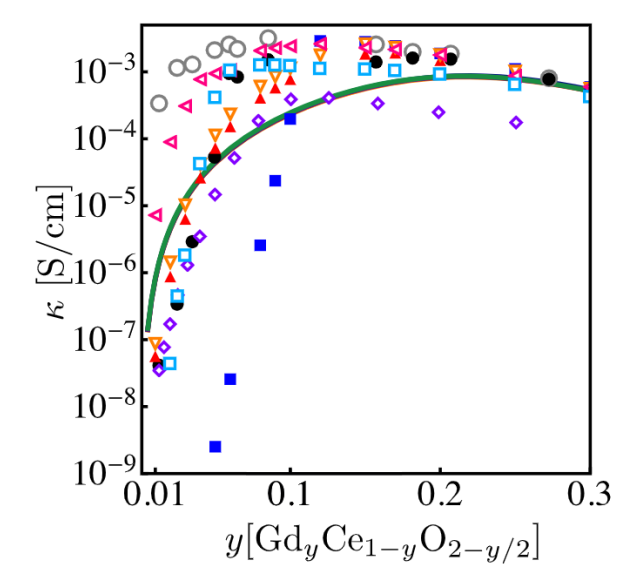


Fig. 4. Macroscopic ionic conductivity as a function of GCO dopant for each described model optimized to fit the experimental data (see Table 2). Experimental data corresponds to ○ for single-crystal GCO and ○ for polycrystalline GCO [77]. Model results correspond to ○ for DH, ○ for MS, ○ for SGC, ○ for AGC, ○ for MDS, and △ for VCG. In addition, ○ shows VCG without mechanical effects, ○ shows VCG with gradient energies, □ shows MDS fitted with resistor-circuit conductivity model, and ○ shows conductivity values reported in [19] that were fitted using MDS and a model for oxygen-ion conductivity in doped fluorite electrolytes given by Nakayama and Martin [93]. Optimization of the parameters in Table 2 give the appearance of a small error without capturing the actual physics of the SCL, highlighting the sensitivity of the models to the accuracy of measured values.

**Table 2**Summary of parameters changed from Table 1 so that the polycrystalline conductivity would match experimental results. Parameters unlisted here remained unchanged.

Symbol	DH	MS	SGC	AGC	MDS	VCG	Units
$\alpha_{a}$	_	_	_	-	0.15	0.05	eV nm²
$\alpha_{ extsf{v}}$	_	_	_	_	0.1	0.0023	eV nm <sup>2</sup>
$oldsymbol{\phi}_\circ$	0.239	0.226	0.276	0.189	_	_	V

**Table 3** Summary of root mean square error calculated using Eq. (20). Reported error% (err% = err/100) corresponds to parameters reported in Table 1, whereas error for optimized models correspond to parameters reported in Table 2.  $^{\dagger}$ VCG reported uses the mechanical energy contribution, whereas the fitted value uses gradient energy

Model	Reported %	Fitted %
DH	13.456	6.654
MS	16,302	6.654
SGC	7.562	6.653
AGC	24.139	6.656
MDS	12.78	0.549
VCG <sup>†</sup>	1.77	1.79
$VCG_{F^{xs}=0}$	4.536	_

tions,  $F_{add}$ , was quantified to explore the changes in total electrical conductivity. Without any additional free energy contributions (i.e.,  $F_{add}=0$ ), both VCG and MDS models fall short in predicting the drop in conductivity at low gadolinium concentrations. They show the general trend for conductivity and thus contribute a lower error than the ideal solution models. In the absence of mechanical stresses and addition of gradient energy penalties (shown in Table 2) of  $F_{add}$  in modified VCG model shows a lower cumulative error than MDS and VCG models.

An analysis was made on the impact of the segregation energy term, which is a dominating factor in the defect concentration within the grain boundary. This parameter has the same effect on all the published strong solution models as  $\phi_{\circ}$  does for the ideal solution models, which is to be expected because the interfacial potential is proportional to the interfacial chemical potential,  $\phi_{\circ} = \frac{\xi_i}{Z_i \nu_i e}$ , and thus the segregation energy. In this context,  $\phi_{\circ}$  could be tuned for the ideal solution models, when  $f_{V_0^{\circ}}^{\circ} - f_{V_0^{\circ}}^{\infty}$  is varied slightly, and conductivity prediction will change drastically, as shown in Fig. 5.

If VCG is used without any additional free energy term (i.e.,  $F_{add}=0$ ), as the segregation energy favors oxygen vacancy accumulation in the grain boundary, the total conductivity decreases, due to a larger depletion zone of oxygen vacancies. The opposite effect occurs when  $f_{\rm Gd'_{Ce}}^{\circ}-f_{\rm Gd'_{Ce}}^{\infty}$  decreases. If gadolinium prefers the grain

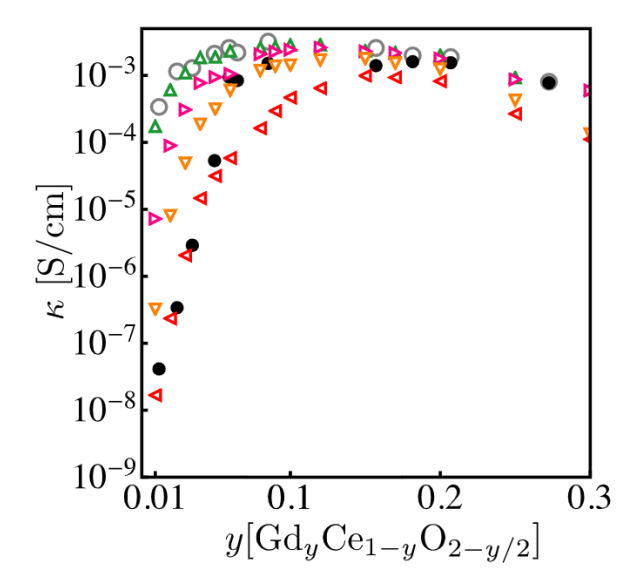


**Fig. 5.** Macroscopic ionic conductivity as a function of dopant concentration in GCO for VCG with no  $F_{add}$ . Experimental data corresponds to  $\bigcirc$  for single-crystal GCO and  $\bigcirc$  for polycrystalline GCO [77]. Model results correspond to a segregation energy,  $f_{V_0}^{\circ} - f_{V_0}^{\infty}$  (eV/atom), of -1 for  $\triangle$ , -2 for  $\checkmark$ , and -3.5 for  $\checkmark$ . Similar to how the core voltage,  $\phi_{\circ}$ , can be varied systematically to better fit experimental conductivity for the ideal solution models, the segregation energy can also be adapted to improve the fit of strong solution models.

**Table 4**Summary of conductivity error for VCG for various oxygen vacancies segregation energies.

$f_{V_{0}^{\circ}}^{\circ} - f_{V_{0}^{\circ}}^{\infty}$	-1	-2	-3	-3.5	eV/atom
error % (Eq. (20))	6.01	4.54	2.83	1.91	_

boundary core to the bulk, the interfacial voltage,  $\phi_{\circ}$ , decreases and the bulk electrical conductivity increases. However, in the absence of experimental data,  $f_{V_{0}^{\circ}}^{\circ} - f_{V_{0}^{\circ}}^{\infty}$  becomes another fitting parameter that can be used to adjust any proposed model, regardless of its validity, as shown in Table 4.

Fig. 6 highlights the effect of the different models on the resultant concentration profiles for gadolinium site fraction of y=0.01. By construction, ideal solution models displaying infinitely thin grain boundaries result in a discontinuity in the interfacial voltage and composition, thus leading to infinitely large charge gradients at the grain boundary core. This assumption is common in analytical solutions, but does not allow to capture any features pertaining to the grain boundary core and its impact on SCL in the abutting grains. In addition, AGC has an additional discontinuity between the SCL and the bulk due to extrinsic material effects.

In contrast, MDS and VCG models avoid discontinuities by specifying a symmetric boundary condition with a slope of zero at the center of the grain boundary (specified as x=0). Due to the gradient energy coefficient,  $\alpha_i$ , MDS shows large concentration gradients on the order of a few Angstroms. VCG has no such sharp concentration gradients due to the large mechanical energy contributions that would result at the interface. However, a large gradient energy coefficient would suppress concentration gradients in any phase field model formulation [32], and inhibit the naturally occurring phase transitions.

For higher concentrations of gadolinium, *i.e.*, y = 0.1, Fig. 7 shows the profiles of concentration of defects, charge density, and electrostatic potentials (see Table 1 for used model parameters). Here, the defect concentration profiles display discontinuities, only a few unit cells wide, breaking the assumption of model continuity

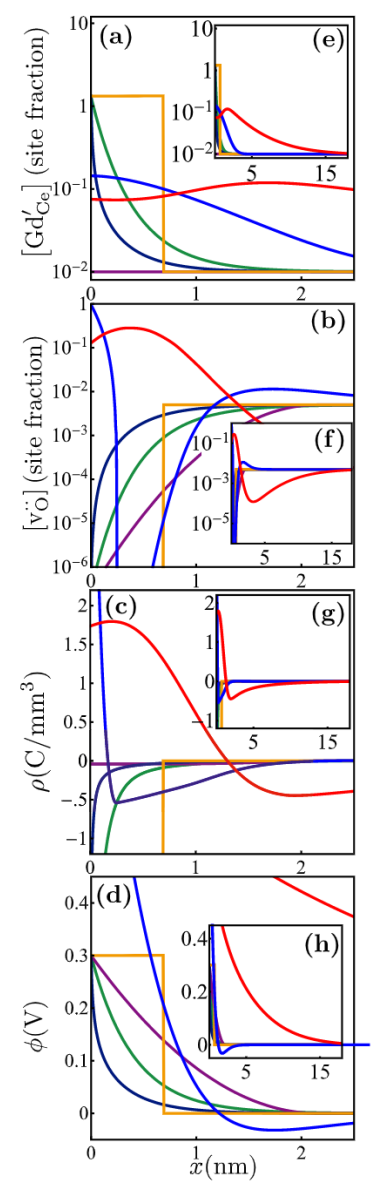


**Fig. 6.** For a bulk gadolinium dopant site fraction of y=0.01 in  $Gd_yCe_{1-y}O_{2-y/2}$ , (a,e) corresponds to the site fraction of gadolinium defects, (b,f) to the site fraction of oxygen vacancies, (c,g) to charge density, and (d,h) to electrostatic potential as a function of distance away from the grain boundary core. Insets (e-h) have the same axis as their larger counterparts, but show the extent of the SCL for the strong solution models. — corresponds to DH, — to MS, — to SGC, — to AGC, — to MDS, and — to VCG. Calculations show that close to the grain boundary, the ideal solution models predict extremely small lengths for the SCL.

in those models that display it. Additionally, near the grain boundary, the site fraction of gadolinium exceeds a value of unity, which is unphysical. At this high site fraction, the differences between MDS and VCG models are appreciable. The MDS model appears to have a discontinuity at around x = 0.04 nm and predicts a drop of several orders of magnitude in oxygen vacancy site fraction within a single unit cell, which also breaks the assumption of continuity. In contrast, the VCG model has no such discontinuity, and predicts a SCL of over 5 nm in width. This prediction is on the same order of magnitude, as experimental reports [16,80,100–102]. Further, [80] reported that the SCL varies with crystallographic misorientation at the grain boundary and this effect has been reproduced by using the VCG approach by Vikrant and coworkers, [29].

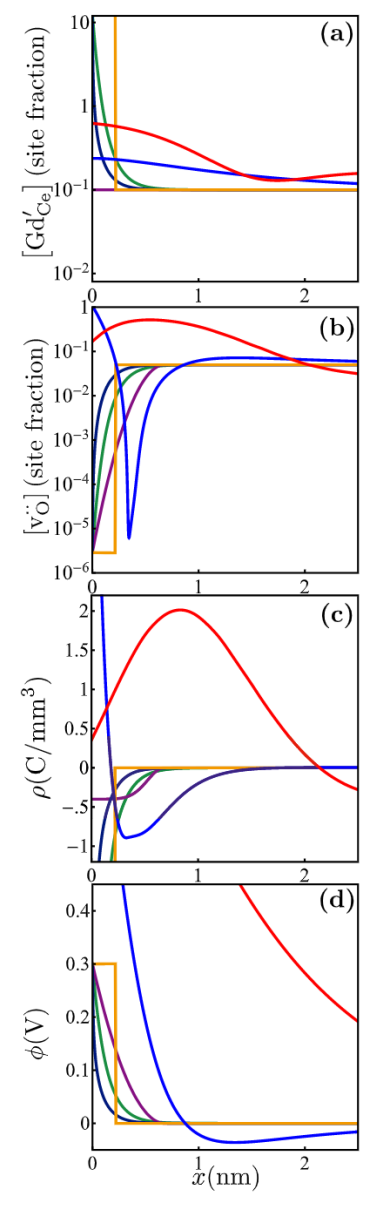


**Fig. 7.** For a bulk gadolinium dopant concentration of y = 0.10 in  $Gd_yCe_{1-y}O_{2-y/2}$ , (a) corresponds to defect concentration of gadolinium, (b) corresponds to defect concentration of oxygen vacancies, (c) corresponds to charge density, and (d) corresponds to electrostatic potential as a function of distance away from the grain boundary core. — corresponds to DH, — to MS, — to SGC, — to AGC, — to MDS, and — to VCG. At higher dopant concentration, the SCL is modeled as only a few atomic layers thick. Conductivity loss in such a short SCL is due to the fact that all models except VCG have a layer of atoms of almost no oxygen vacancies.

### 5. Summary and conclusions

A thermodynamically consistent variational framework has been presented that can encapsulate both analytical ideal solution models and strong solution descriptions, including the effects of structure, stress, and the multiphysical behavior that occurs in real material systems. In general, DH, MS, SGC, and AGC models are unable to capture the physical effects of the SCL in a highly doped system, regardless of their ability to correctly predict the conductivity [56]. The DH, SGC, and AGC models describe accurately intrinsic systems, whereas MS is limited to lightly doped systems with immobile charge carriers. SCLs of length less than 2 nm can be predicted, which is not realistic for ionic materials. The MDS model provides a good fit to experimentally observed conductivity,

but the defect gradients shown in Fig. 7(b) are unphysically sharp across one lattice parameter. VCG incorporates the contributions of mechanical energy due to chemical expansion of excess defects in the lattice, a well-known phenomenon in the ceramics, metals, polymers, and semiconductors literature, and allows to accurately describe a thick SCL of 20 nm, without introducing any unmeasurable parameters. Instead, the resultant thick SCL favorably contributes to accurately describe the total electrical conductivity of polycrystals by using only experimentally measurable physical quantities. Further, the model has the capability to predict the SCL and electrical conductivity as a function of crystallographic misorientation [29], and sets the stage to understand grain growth and sintering in ionic ceramics.

Overall, a comprehensive thermodynamically-consistent framework for space charge and segregation enables the multiphysical description of grain boundaries and interfaces, and would be a valuable tool for microstructure design, including grain size, grain boundary character and crystallographic texture optimization. Ultimately, any proposed formulation demands constant tests to their validity and versatility to capture the physics of other material applications. Additionally, model validation requires experimental data of more than just one physical parameter, e.g., SCL length, effect of grain size on electrical conductivity, etc. In this context, the framework allows to computationally analyze less known and more complicated multi-component systems to predict materials properties and evaluate the effect of external thermal, chemical, mechanical, electrical and magnetic stimuli to tailor the interfacial properties for a given application.

## **Declaration of Competing Interest**

The authors declare that they have no known competing financial interests or personal relationships that could have appeared to influence the work reported in this paper.

## Acknowledgments

JL and REG thank the support provided by Toyota Research Institute. KSNV and REG thank the support provided by US ONR N00014-17-1-2087. REG acknowledges the support from NSF DMR 1734763. WR thanks support by the DFG via the Emmy Noether Programme no. Rh 146/1-1.

#### Appendix A. Symbols

Glossary of symbols.

Name	Definition	Units
С	Concentration of defects in SGC	mol/m³
C <sub>ijkl</sub> Ď	Component of stiffness matrix	N/m <sup>2</sup>
D	Electric displacement vecter	C m
$D_i^{\circ}$	Self-diffusion coefficient of i-th species	m <sup>2</sup> /s
$D_{i}^{\circ}$ $D_{V_{O}}^{\circ}$ $E_{a,i}$	Self-diffusion coefficient of oxygen vacancies	m <sup>2</sup> /s
$E_{a,i}$	Activation energy of ith species for migration	eV
$E_{a,V_{O}}$	Activation energy of oxygen vacancies for migration	eV
е	Electronic charge	C
Ē	Electric Field	v/m
Ε	Modulus of elasticity	Gpa
F	Total Helmholtz free energy	J
$F_{add}$	Free energy contributions besides electrochemical	J
$\mathcal{F}$	Faraday's constant	C/mol
f	Helmholtz free energy density	J/m <sup>3</sup>
$f_{ec}$	Electrochemical free energy density of the system	J/m <sup>3</sup>
$f_{vol}$	Volumetric Helmholtz free energy density	J/m³
$f_i$	Formation energy of i-th defect	J/m³
$f_i^{\circ} - f_i^{\infty}$	Segregation energy of i-th defect to gb	eV
$f_{V_{\ddot{o}}}^{\circ} - f_{V_{\ddot{o}}}^{\infty}$	Segregation energy of oxygen vacancies	eV

(continued on next page)

Table A1 (continued)

Name	Definition	Units
$f_{Gd'_{Ce}}^{\circ} - f_{Gd'_{Ce}}^{\infty}$	Segregation energy of gadolinium defects	eV
$\Delta G_{mix}$	Gibbs free energy of mixing	J/m <sup>3</sup>
$\Delta H_{mix}$	Enthalpy of mixing	J/m³
$k_B$	Boltzmann constant	eV/atom
M	Number of phase	_
N	Number of charged species	-
n	Number of measurements	-
$\Delta S_{mix}$	Entropy of mixing	J/(m <sup>3</sup> K)
S	Entropy	J/(m <sup>3</sup> K)
5	Entropy density	J/(m <sup>3</sup> K)
R	Universal gas constant	J/(mol K)
err	Root mean square error	_
Γ,	Temperature	K
/	Volume of the system	m <sup>3</sup>
/i	Site fraction of the ith defect	-
′i,∞	Site fraction of the <i>i</i> th defect in the bulk	-
/im	Site fraction of the major immobile charge carrier	177
/m,0	Stress free site fraction of the mth defect	-
ζ	Distance from the center of the grain boundary	nm
ī	Mechanical displacement	nm
k	kth controlling variable	5
$Z_i$	Charge number or valence of the <i>i</i> -th defect	=
$Z_0$	Oxygen vacancies ionic valence	-
Gd	Gadolinium defects ionic valence	-
im	Charge number of the major immobile charge carrier	-
$x_i$	Gradient energy coefficient of ith defect	eV nm <sup>2</sup>
3m	ijth component of Vegard tensor of mth species	-
3(0)	Vegard expansion constant of oxygen vacancies	-
B(Gd)	Vegard expansion constant of gadolinium defects	-
6	Thickness of the grain boundary (VCG)	nm
Fo.	Permittivity of free space	F/m
r	Relative dielectric constant	-
e	Elastic strain	177
<sup>©</sup> kl	klth component of total strain	-
k	Generalized contribution of the kth potential	$J/m^3$
7	Order parameter in phase field	-
, 1 <sub>0</sub>	Disorder at the gb	-
c	Conductivity	S/cm
	Grain size	nm
Db	Debye length	nm
*	Mott-Schottky Length	nm
i	Generalized electrochemical potential of ith	J/mol
	species	
ŝi	Classical electrochemical potential of ith species	J/mol
$u_i^f$	Standard chemical potential from ith defect	J/mol
1	formation	31
$\tilde{u}_i$	Equilibrium chemical potential of ith defect	J/mol
$\nu_i$	Molar site volume of sublattice where ith defect	m³/mol
•	resides	
$\nu_{\circ}$	Area-specific molar site density	m <sup>2</sup> /mol
v	Poisson ratio	- 1
0	Charge density	C/m <sup>3</sup>
J	Elastic stress tensor	N/m <sup>2</sup>
ν Vii	ij-th component of stress tensor	N/m <sup>2</sup>
<i>p</i>	Electrostatic potential referenced to the bulk	V
$\phi_{\circ}$	Electrostatic potential at the gb	V
$\phi_{\infty}$	Bulk electrostatic potential	V
F 000	Interaction energy between ith and jth defect	J/mol
$\Omega_{ij}$	interaction energy between an and an defect	1/11101

#### Appendix B. Model derivations

B1. Generalities to deriving historical models from a free energy functional

Define f as an ideal free energy with each defect on a separate sublattice,

$$f(y_1, y_2, T) = \frac{1}{\nu_1} \left( f_1(T) y_1 + RT y_1 \ln(y_1) + RT (1 - y_1) \ln(1 - y_1) \right) + \frac{1}{\nu_2} \left( f_2(T) y_2 + RT y_2 \ln(y_2) + RT (1 - y_2) \ln(1 - y_2) \right).$$
(B.1)

If the defects are dilute,  $\ln (1-y_i) = 0$ . Using Eq. (2), the variational derivative of F,

$$v_i \frac{\delta F}{\delta y_i} = f_i(T) + RT \ln(y_i) + Z_i \mathcal{F} \phi, \tag{B.2}$$

is spatially uniform at equilibrium.

Additionally, the variational derivative of F with respect to  $\phi$  is

$$\frac{\delta F}{\delta \phi} = Z_1 \mathcal{F} y_1 / \nu_1 + Z_2 \mathcal{F} y_2 / \nu_2 + \epsilon \nabla^2 \phi = 0, \tag{B.3}$$

at equilibrium. Eq. (B.3) constitutes the basis to describe DH, MS, SGC, and AGC models.

#### B2. Debye-Hückel (DH) model

The underlying assumption for DH is that for high temperatures and small electrostatic fields,  $\exp\left[-Z_i\mathcal{F}\phi(x)/RT\right]\sim 1-Z_i\mathcal{F}\phi(x)/RT$ . Eq. (1) is then simplified to Eq. (8) [1].

#### B3. Mott-Schottky (MS)

MS neglects all defects except one major, immobile charge carrier, which simplifies Eq. (1) into Eq. (10). Note that  $y_{im}$  is constant spatially as a result of its immobility. Eq. (10) is solved with boundary conditions:  $\phi(0) = \phi_o$ ,  $\phi(\lambda^*) = 0$  and  $\phi'(\lambda^*) = 0$ , where  $\lambda^*$  is the edge of the space charge layer. Eq. (11) is for  $\phi(x>0)$  At x=0,  $d^2\phi/dx^2$  is undefined because the model neglects other defects [4].

#### B4. Symmetric Gouy-Chapman (SGC)

SGC considers a two defect system of equal and opposite charge (*i.e.*,  $Z=Z_+=-Z_-$ ) is considered. Since there is electroneutrality in the bulk,  $\xi(x)=\frac{y_+}{\nu_+}=\frac{y_-}{\nu_-}$ . Thus, Eq. (13) leads to Eq. (14) for intrinsic systems.

## B5. Mebane-DeSouza (MDS)

MDS does not provide a free energy functional (see Eq. (16)) [19]. They do, however, define the electrochemical potential as

$$\tilde{\mu}_{\nu} = \mu_{\nu}^{f} + \Omega_{\nu\nu} y_{\nu} + \Omega_{a\nu} y_{a} + RT \ln \left( \frac{y_{\nu}}{1 - y_{\nu}} \right) + Z_{\nu} \mathcal{F} \phi - \alpha_{\nu} \nabla^{2} y_{\nu}$$
(B.4)

$$\begin{split} \tilde{\mu}_{a} &= \mu_{a}^{f} + \Omega_{aa} \mathsf{y_a} + \Omega_{a\nu} \mathsf{y_v} + RT \ln \left( \frac{\mathsf{y_a}}{1 - \mathsf{y_a}} \right) + Z_{a} \mathcal{F} \phi - \alpha_{a} \nabla^{2} \mathsf{y_a} \end{split} \tag{B.5}$$

for a two-defect system: a dopant, a, and vacancies,  $\nu$ .  $\Omega_{ij}$  is the interaction energy between the ith and jth species and  $\alpha_i$  is the gradient energy coefficient [47]. While a separate paper by Mebane [99] was cited for the corresponding free energy functional, the two papers do not agree, and it is not possible to infer the functional from Eqs. (B.4) and (B.5).

#### B6. Vikrant-Chueh-García (VCG)

By using the thermochemical free energy density,

$$f(\eta, \{y_i\}, T) = \frac{1}{\nu} \sum_{i=1}^{N} \left( f_i(\eta, T) y_i + RT y_i \ln(y_i) + RT (1 - y_i) \ln(1 - y_i) + \sum_{j=1, i \neq j}^{N} \Omega_{ij} y_i y_j \right),$$
(B.6)

where  $\Omega_{ij}$  are the interaction energies between species, and substituting into the fundamental variational principle, Eq. (6), one readily finds Equation set (7).

#### Supplementary material

Supplementary material associated with this article can be found, in the online version, at doi:10.1016/j.actamat.2020.116525

#### References

- [1] G. Gregori, R. Merkle, J. Maier, Ion conduction and redistribution at grain boundaries in oxide systems, Prog. Mater. Sci. 89 (2017) 252-305.
- [2] B.V. Lotsch, J. Maier, Relevance of solid electrolytes for lithium-based batteries: a realistic view, J. Electroceram. 38 (2) (2017) 128-141.
- [3] X. Guo, R. Waser, Electrical properties of the grain boundaries of oxygen ion conductors: acceptor-doped zirconia and ceria, Prog. Mater. Sci. 51 (2) (2006) 151-210
- [4] M.C. Göbel, G. Gregori, J. Maier, Numerical calculations of space charge layer effects in nanocrystalline ceria, Part I: comparison with the analytical models and derivation of improved analytical solutions, Phys. Chem. Chem. Phys. 16 (21) (2014) 10214-10231.
- [5] M.C. Göbel, G. Gregori, J. Maier, Numerical calculations of space charge layer effects in nanocrystalline ceria, Part II: detailed analysis of the space charge layer properties, Phys. Chem. Chem. Phys. 16 (21) (2014) 10175-10186.
- [6] P. Balaya, A.J. Bhattacharyya, J. Jamnik, Y.F. Zhukovskii, E.A. Kotomin, J. Maier, Nano-ionics in the context of lithium batteries, J. Power Sources 159 (2006) 171-178. 1 SPEC. ISS.
- A. Kayyar, H. Qian, J. Luo, Surface adsorption and disordering in LiFePO<sub>4</sub> based battery cathodes, Appl. Phys. Lett. 95 (22) (2009) 221905.
- [8] C. Ma, K. Chen, C. Liang, C.W. Nan, R. Ishikawa, K. More, M. Chi, Atomic-scale origin of the large grain-boundary resistance in perovskite Li-ion-conducting solid electrolytes, Energy Environ. Sci. 7 (5) (2014) 1638-1642.
- [9] J. Luo, Interfacial engineering of solid electrolytes, J. Materiomics 1 (1) (2015)
- [10] J. Maier, On the conductivity of polycrystalline materials, Berich Bunsen Gese 00 (1) (1986) 26–33.
- [11] X. Guo, S. Mi, R. Waser, Nonlinear electrical properties of grain boundaries in oxygen ion conductors: acceptor-doped ceria, Electrochem, Solid-State Lett, 8 (1) (2005) [1-[3.
- [12] X. Guo, Physical origin of the intrinsic grain-boundary resistivity of stabilized-zirconia: role of the space-charge layers, Solid State Ion. 81 (3) (1995)
- [13] X. Guo, J. Maier, Grain boundary blocking effect in zirconia: aSchottky barrier analysis, J. Electrochem. Soc. 148 (3) (2001) E121-E126.
- [14] M. Shirpour, B. Rahmati, W. Sigle, P.A. Van Aken, R. Merkle, J. Maier, Dopant segregation and space charge effects in proton-conducting bazro<sub>3</sub> perovskites, J. Phys. Chem. C 116 (3) (2012) 2453–2461.
- [15] W.D. Callister, D.G. Rethwisch, Fundamentals of Materials Science and Engineering, fourth ed., Wiley, 2011.
- [16] M. Aoki, Y.-M. Chiang, I. Kosacki, L.-R. Lee, H. Tuller, Y. Liu, Solute segregation and grain-boundary impedance in high-purity stabilized zirconia, J. Am. Ceram. Soc. 79 (1996) 1169-1180.
- [17] L. Priester, Grain Boundaries from Theory to Engineering, Springer Science & Business Media, 2013.
- [18] K.L. Kliewer, J.S. Koehler, Space charge in ionic crystals. I. General approach with application to NaCl, Phys. Rev. 140 (4A) (1965) A1226-A1240.
- [19] D.S. Mebane, R.A. De Souza, A generalised space-charge theory for extended defects in oxygen-ion conducting electrolytes; from dilute to concentrated solid solutions, Energy Environ. Sci. 8 (10) (2015) 2935-2940.
- [20] J.D. Jackson, Classical Electrodynamics, Wiley, New York, 1975.
   [21] V. Steffen, L. Cardozo-Filho, E.A. Silva, L.R. Evangelista, R. Guirardello, M.R. Mafra, Equilibrium modeling of ion adsorption based on Poisson-Boltzmann equation, Colloids Surf. A 468 (2015) 159-166.
- [22] C. Ang, Z. Yu, DC electric-field dependence of the dielectric constant in polar dielectrics: multipolarization mechanism model, Phys. Rev. B 69 (17) (2004) 174109.
- [23] J. Li, F. Li, C. Li, G. Yang, Z. Xu, S. Zhang, Evidences of grain boundary capacitance effect on the colossal dielectric permittivity in (Nb+In) co-doped TiO<sub>2</sub> ceramics, Sci. Rep. 5 (1) (2015) 8295.
- [24] A. Cho, C.S. Han, M. Kang, W. Choi, J. Lee, J. Jeon, S. Yu, Y.S. Jung, Y.S. Cho, Direct correlations of grain boundary potentials to chemical states and dielections. tric properties of doped CaCu<sub>3</sub>Ti<sub>4</sub>O<sub>12</sub> thin films, ACS Appl. Mater. Interfaces 10 (18) (2018) 16203–16209.
- [25] T. Hiramatsu, T. Tamura, N. Wada, H. Tamura, Y. Sakabe, Effects of grain boundary on dielectric properties in fine-grained batio<sub>3</sub> ceramics, Mater. Sci. Eng. BSolid-State Mater. Adv. Technol. 120 (1-3) (2005) 55-58.
- [26] J.W. Gibbs, On the equilibrium of heterogeneous substances, Phys. Rev. 16 (96) 1878) 441-458.
- [27] J.W. Cahn, On spinodal decomposition, Acta Metall. 9 (1961) 795-801.
- [28] S.M. Allen, J.W. Cahn, A microscopic theory for antiphase boundary motion and its application to antiphase domain coarsening, Acta Metall. 27 (1979) 1085-1095

- [29] K.S.N. Vikrant, R.E. García, Charged grain boundary transitions in ionic ceramics for energy applications, npj Comput. Mater. 5 (1) (2019) 24.
- [30] S. Kim, J. Fleig, J. Maier, Space charge conduction: simple analytical solutions for ionic and mixed conductors and application to nanocrystalline ceria, Phys. Chem. Chem. Phys. 5 (11) (2003) 2268–2273.
- L. Kaufman, CALPHAD-Computer Coupling of Phase Diagrams and Thermo-chemistry, Pergamon Oxford, Oxford, UK, 1977.
- [32] W.J. Boettinger, J.A. Warren, C. Beckermann, A. Karma, Phase-field simulation of solidification, Annu. Rev. Mater. Res. 32 (2002) 163–194.
- [33] L.Q. Chen, Phase-field models for microstructure evolution, Annu. Rev. Mater. Res. 32 (2002) 113-140.
- [34] R. Kobayashi, J.A. Warren, W.C. Carter, A continuum model of grain bound-aries, Phys. D 140 (2000) 141–150.
- [35] J.A. Warren, R. Kobayashi, A.E. Lobkovsky, W.C. Carter, Extending phase field models of solidification to polycrystalline materials, Acta, Mater, 51 (2003) 6035-6058
- [36] B. Sundman, J. Ågren, A regular solution model for phases with several components and sublattices, suitable for computer applications, J. Phys. Chem. Solids 42 (4) (1981) 297–301.
- [37] K.S.N. Vikrant, W.C. Chueh, R.E. García, Charged interfaces: Electrochemical and mechanical effect, Energy Environ. Sci. 11 (2018) 1993–2000.
- [38] C.H.P. Lupis, Chemical thermodynamics of materials, Elsevier Science Publishing Co., North Holland, New York, USA, 1983.
- [39] R. DeHoff, Thermodynamics in materials science, second ed., CRC Press, Boca Raton, 2006.
- [40] H. Lukas, S.G. Fries, B. Sundman, Computational Thermodynamics: The Calphad Method, Cambridge University Press, 2007.
- [41] R.M. Horton, A.J. Haslam, A. Galindo, G. Jackson, M.W. Finnis, New methods for calculating the free energy of charged defects in solid electrolytes, J. Phys. Condens, Matter 25 (39) (2013) 395001.
- [42] D.L. Chapman, LI. a contribution to the theory of electrocapillarity, London, Edinburgh, Dublin, Philos. Mag. J. Sci. 25 (148) (1913) 475–481.
- M. Gouy, Sur la constitution de la charge électrique à la surface d'un électrolyte, J. Phys. Théor. Appl. 9 (1) (1910) 457-468.
- [44] N.F. Mott, The theory of crystal rectifiers, Proc. R. Soc. A 171 (944) (1939) 27\_38
- [45] N.F. Mott, Note on the contact between a metal and an insulator or semiconductor, Math. Proc. Camb. Philos. Soc. 34 (4) (1938) 568-572.
- J.D. Eshelby, C.W.A. Newey, P.L. Pratt, A.B. Lidiard, Charged dislocations and the strength of ionic crystals, Philos. Mag. 3 (25) (1958) 75-89.
- J.W. Cahn, J.E. Hilliard, Free energy of a nonuniform system i, interfacial free energy, J. Chem. Phys. 28 (1958) 258-267.
- [48] J.W. Cahn, Free energy of a nonuniform system. II. Thermodynamic basis, J. Chem. Phys. 30 (1959) 1121-1124.
- E.W. Hart, Thermodynamics of inhomogeneous systems, Phys. Rev. 113 (1959) 412-416.
- [50] O. Penrose, P.C. Fife, Thermodynamically consistent models of phase-field
- type for the kinetics of phase transitions, Phys. D 43 (1990) 44-62 J.E. Guyer, W.J. Boettinger, J.A. Warren, G.B. McFadden, Phase field modeling
- of electrochemistry I: equilibrium, Phys. Rev. E. 69 (2004) 021603 [52] J.E. Guyer, W.J. Boettinger, J.A. Warren, G.B. McFadden, Phase field modeling of electrochemistry II: kinetics, Phys. Rev. E. 69 (2004) 021604.
- [53] R.E. García, C.M. Bishop, W.C. Carter, Thermodynamically consistent variational principles with applications to electrically and magnetically active systems, Acta Mater. 52 (1) (2004) 11-21.
- [54] C.M. Bishop, R.E. García, W.C. Carter, Effect of charge separation on the stability of large wavelength fluctuations during spinodal decomposition, Acta Mater. 51 (6) (2003) 1517-1524.
- [55] R.T. DeHoff, Thermodynamics in Materials Science, McGraw-Hill, New York,
- [56] P.B.V. Weg, The electrochemical potential and ionic activity coefficients. A possible correction for Debye-Hückel and Maxwell-Boltzmann equations for dilute electrolyte equilibria, J. Colloid Interface Sci. 339 (2) (2009) 542–544.
- [57] R.S. Qin, H.K. Bhadeshia, Phase field method, Mater. Sci. Technol. 26 (7) (2010) 803-811.
- [58] J.F. Nye, Physical Properties of Crystals, Oxford University Press, Oxford, UK,
- [59] W.C. Carter, J.E. Taylor, J.W. Cahn, Variational methods for microstructural evolution theories, J. Mater. 49 (1997) 30-36.
- [60] Z. Suo, Motions of microscopic surfaces in materials, Adv. Appl. Mech. 33 1997) 193-294.
- [61] Y.C. Shiu, K. Bhattacharya, Domain patterns and macroscopic behavior of ferroelectric materials, Philos. Mag. B 81 (12) (2001) 2021-2054.
- V. Steffen, E.A. Silva, L.R. Evangelista, L. Cardozo-Filho, Debye-Hückel approximation for simplification of ions adsorption equilibrium model based on Poisson-Boltzmann equation, Surf. Interfaces 10 (2018) 144-148.
- [63] F. Larche, J.W. Cahn, A linear theory of thermochemical equilibrium of solids under stress, Acta Metall. 21 (1973) 1051-1063.
- [64] J.W. Cahn, Transition and phase equilibria among grain boundary structures, J. Phys. 43 (1982). C6–199–C6–213
- [65] J.W. Cahn, Critical point wetting, J. Chem. Phys. 66 (1977) 3667-3672.
- M. Tang, W.C. Carter, R.M. Cannon, Grain boundary transitions in binary alloys, Phys. Rev. Lett. 97 (2006) 075502.
- [67] P. Debye, E. Huckel, Zur theorie der elektrolyte, Phys. Z. 24 (1923) 185-206.
- K. Lehovec, Space-charge layer and distribution of lattice defects at the surface of ionic crystals, J. Chem. Phys. 21 (7) (1953) 1123–1128.

- [69] J. Maier, Ionic conduction in space charge regions, Prog. Solid State Chem. 23 (3) (1995) 171–263.
- [70] S.K. Tiku, F.A. Kröger, Effects of space charge, grain-boundary segregation, and mobility differences between grain boundary and bulk on the conductivity of polycrystalline Al<sub>2</sub>O<sub>3</sub>, J. Am. Ceram. Soc. 63 (3-4) (1980) 183–189.
- [71] G.H. Bolt, Analysis of the validity of the Gouy-Chapman theory of the electric double layer, J. Colloid Sci. 10 (2) (1955) 206–218.
- [72] S.K. Kim, S. Khodorov, I. Lubomirsky, S. Kim, A linear diffusion model for ion current across blocking grain boundaries in oxygen-ion and proton conductors, Phys. Chem. Chem. Phys. 16 (28) (2014) 14961–14968.
- [73] W. Schottky, Zur halbleitertheorie der sperrschicht- und spitzengleichrichter, Z. Phys. 113 (5) (1939) 367–414.
- [74] B. Wang, Z. Lin, A schottky barrier based model for the grain size effect on oxygen ion conductivity of acceptor-doped zro<sub>2</sub> and CeO<sub>2</sub>, Int. J. Hydrog. Energy 39 (26) (2014) 14334–14341.
- [75] S. Kim, S.K. Kim, S. Khodorov, J. Maier, I. Lubomirsky, On determining the height of the potential barrier at grain boundaries in ion-conducting oxides, Phys. Chem. Chem. Phys. 18 (4) (2016) 3023–3031.
- [76] G.M. Torrie, J.P. Valleau, Electrical double layers. 4. limitations of the Gouy-Chapman theory, J. Phys. Chem. 86 (16) (1982) 3251–3257.
- [77] A. Tschöpe, S. Kilassonia, R. Birringer, The grain boundary effect in heavily doped cerium oxide, Solid State Ion. 173 (2004) 57–61.
- [78] D.P. Thompson, A.M. Dickins, J.S. Thorp, The dielectric properties of zirconia, J. Mater. Sci. 27 (8) (1992) 2267–2271.
- [79] S. Grieshammer, B.O. Grope, J. Koettgen, M. Martin, A combined DFT + U and Monte Carlo study on rare earth doped ceria, Phys. Chem. Chem. Phys. 16 (21) (2014) 9974–9986.
- [80] K. Yasuda, K. Uemura, T. Shiota, Sintering and mechanical properties of gadolinium-doped ceria ceramics, in: J. Phys. Conf. Ser., Vol. 339, IOP Publishing, 2012, p. 012006.
- [81] S. Zha, C. Xia, G. Meng, Effect of Gd (Sm) doping on properties of ceria electrolyte for solid oxide fuel cells, J. Power Sources 115 (1) (2003) 44–48.
- [82] Y. Lin, S. Fang, D. Su, K.S. Brinkman, F. Chen, Enhancing grain boundary ionic conductivity in mixed ionic-electronic conductors, Nat. Commun. 6 (1) (2015) 6824
- [83] W.R. Inc, Mathematica, Version 12.1, Champaign, IL (2020). https://www.wolfram.com/mathematica.
- [84] 2018. MATLAB, 9.7.0.1190202 (R2019b), The MathWorks Inc., Natick, Massachusetts.
- [85] A.C.E. Reid, R.C. Lua, R.E. García, V.R. Coffman, S.A. Langer, Modelling microstructures with oof2, Int. J. Mater. Prod. Technol. 35 (2009) 361–373.
- [86] J.E. Guyer, D. Wheeler, J.A. Warren, FiPy: partial differential equations with python, Comput. Sci. Eng. 11 (2009) 615.
- [87] S. Kim, J. Maier, On the conductivity mechanism of nanocrystalline ceria, J. Electrochem. Soc. 149 (10) (2002) J73.

- [88] M.C. Göbel, G. Gregori, X. Guo, J. Maier, Boundary effects on the electrical conductivity of pure and doped cerium oxide thin films, Phys. Chem. Chem. Phys. 12 (42) (2010) 14351–14361.
- [89] S.J. Litzelman, H.L. Tuller, Measurement of mixed conductivity in thin films with microstructured Hebb-Wagner blocking electrodes, Solid State Ion. 180 (20–22) (2009) 1190–1197.
- [90] A. Tschöpe, Grain size-dependent electrical conductivity of polycrystalline cerium oxide. II: space charge model, Solid State Ion. 139 (3-4) (2001) 267–280.
- [91] M.C. Göbel, G. Gregori, J. Maier, Mixed conductivity in nanocrystalline highly acceptor doped cerium oxide thin films under oxidizing conditions, Phys. Chem. Chem. Phys. 13 (23) (2011) 10940–10945.
- [92] M.C. Göbel, G. Gregori, J. Maier, Size effects on the electrical conductivity of ceria: achieving low space charge potentials in nanocrystalline thin films, J. Phys. Chem. C 117 (44) (2013) 22560–22568.
- [93] M. Nakayama, M. Martin, First-principles study on defect chemistry and migration of oxide ions in ceria doped with rare-earth cations, Phys. Chem. Chem. Phys. 11 (17) (2009) 3241–3249.
- [94] K.S.N. Vikrant, H. Wang, A. Jana, H. Wang, R.E. García, Flash sintering incubation kinetics, npj Comput. Mater. 6 (2020) 98.
   [95] K.S.N. Vikrant, W. Rheinheimer, H. Sternlicht, M. Bäurer, R.E. García, Electro-
- [95] K.S.N. Vikrant, W. Rheinheimer, H. Sternlicht, M. Bäurer, R.E. García, Electrochemically-driven abnormal grain growth in ionic ceramics, Acta Mater. 200 (2020) 727–734.
- [96] K.S.N. Vikrant, W. Rheinheimer, R.E. García, Electrochemical drag effect on grain boundary motion in ionic ceramics, npj Comput. Mater. 6 (165) (2020).
- [97] K.S.N. Vikrant, R.L. Grosso, L. Feng, E.N.S. Muccillo, D.N.F. Muche, G.S. Jawahar-ram, C.M. Barr, A.M. Monterrosa, R.H.R. Castro, R.E. García, K. Hattar, S.J. Dillon, Ultrahigh temperature in situ transmission electron microscopy based bicrystal coble creep in zirconia i: Nanowire growth and interfacial diffusivity, Acta Mater. 199 (2020) 530–541.
- [98] R.L. Grosso, K.S.N. Vikrant, L. Feng, E.N.S. Muccillo, D.N.F. Muche, G.S. Jawaharram, C.M. Barr, A.M. Monterrosa, R.H.R. Castro, R.E. García, K. Hattar, S.J. Dillon, Ultrahigh temperature in situ transmission electron microscopy based bicrystal coble creep in zirconia II: interfacial thermodynamics and transport mechanisms, Acta Mater. 200 (2020) 1008–1021.
- [99] D.S. Mebane, A variational approach to surface cation segregation in mixed conducting perovskites, Comput. Mater. Sci. 103 (2015) 231–236.
- [100] J. Maier, Complex oxides: high temperature defect chemistry vs. low temperature defect chemistry, Phys. Chem. Chem. Phys. 5 (11) (2003) 2164–2173.
- [101] W. Rheinheimer, M. Bäurer, C.A. Handwerker, J. Blendell, M. Hoffmann, Growth of single crystalline seeds into polycrystalline strontium titanate: anisotropy of the mobility, intrinsic drag effects and kinetic shape of grain boundaries, Acta Mater. 95 (2015) 111–123.
- [102] W. Rheinheimer, M.J. Hoffmann, Grain growth in perovskites: what is the impact of boundary transitions? Curr. Opin. Solid State Mater. Sci. 20 (5) (2016) 286–298.